Smartphone-based Real Time Vehicle Tracking in Indoor Parking Structures

Ruipeng Gao, *Member, IEEE,* Mingmin Zhao, Tao Ye, Fan Ye, Yizhou Wang, Guojie Luo, *Member, IEEE*

Abstract— Although location awareness and turn-by-turn instructions are prevalent outdoors due to GPS, we are back into the darkness in uninstrumented indoor environments such as underground parking structures. We get confused, disoriented when driving in these mazes, and frequently forget where we parked, ending up circling back and forth upon return. In this paper, we propose VeTrack, a smartphone-only system that tracks the vehicle's location in real time using the phone's inertial sensors. It does not require any environment instrumentation or cloud backend. It uses a novel "shadow" trajectory tracing method to accurately estimate phone's and vehicle's orientations despite their arbitrary poses and frequent disturbances. We develop algorithms in a Sequential Monte Carlo framework to represent vehicle states probabilistically, and harness constraints by the garage map and detected landmarks to robustly infer the vehicle location. We also find landmark (e.g., speed bumps, turns) recognition methods reliable against noises, disturbances from bumpy rides and even hand-held movements. We implement a highly efficient prototype and conduct extensive experiments in multiple parking structures of different sizes and structures, and collect data with multiple vehicles and drivers. We find that VeTrack can estimate the vehicle's real time location with almost negligible latency, with error of $2 \sim 4$ parking spaces at the 80^{th} percentile.

Index Terms—Vehicle real time tracking, indoor environments.

1 Introduction

Thanks to decades of efforts in GPS systems and devices, drivers know their locations at any time outdoors. The location awareness enables drivers to make proper decisions and gives them a sense of "control." However, whenever we drive into indoor environments such as underground parking garages, or multi-level parking structures where GPS signals can hardly penetrate, we lose this location awareness. Not only do we get confused, disoriented in maze-like structures, frequently we do not even remember where we park the car, ending up circling back and forth searching for the vehicle.

Providing real time vehicle tracking capability indoors will satisfy the fundamental and constant cognitive needs of drivers to orient themselves relative to a large and unfamiliar environment. Knowing where they are generates a sense of control and induces calmness psychologically, both greatly enhancing the driving experience. In smart parking systems where free parking space information is available, real time tracking will enable turn-by-turn instructions guiding drivers to those spaces, or at least areas where more spaces are likely available. The final parking location recorded can also be used to direct the driver back upon return, avoiding any back and forth search.

- *R. Gao is with the School of Software Engineering, Beijing Jiaotong University, Beijing 100044, China. Email: rpgao@bjtu.edu.cn*
- *M. Zhao is with the Computer Science and Artificial Intelligence Laboratory, MIT, Cambridge, MA 02142, USA. Email: mingmin@mit.edu*
- *T. Ye, Y. Wang and G. Luo are with the EECS School, Peking University, Beijing 100871, China. Email: {pkuyetao, yizhou.wang, gluo}@pku.edu.cn*
- *F. Ye is with the ECE Department, Stony Brook University, Stony Brook, NY 11794, USA. Email: fan.ye@stonybrook.edu*

However, real time vehicle tracking indoors is far from straightforward. First, mainstream indoor localization technology leverages RF signals such as WiFi [1], [2] and cellular [3], which can be sparse, intermittent or simply non-existent in many uninstrumented environments. Instrumenting the environment [4], [5] unfortunately is not always feasible: the acquisition, installation and maintenance of sensors require significant time, financial costs and human efforts; simply wiring legacy environments can be a major undertaking. The lack of radio signals also means lack of Internet connectivity: no cloud service is reachable and all sensing/computing have to happen locally.

In this paper, we propose VeTrack, a real time vehicle tracking system that utilizes inertial sensors in the smartphone to provide accurate vehicle location. It does not rely on GPS/RF signals, or any additional sensors instrumenting the environment. All sensing and computation occur in the phone and no cloud backend is needed. A driver simply starts the VeTrack application before entering a parking structure, then VeTrack will track the vehicle movements, estimate and display its location in a garage map in real time, and record the final parking location, which can be used by the driver later to find the vehicle.

Such an inertial and phone-only solution entails a series of non-trivial challenges. First, many different scenarios exist for the phone *pose* (i.e., relative orientation between its coordinate system to that of the vehicle), which is needed to transform phone movements into vehicle movements. The phone may be placed in arbitrary positions - lying flat on a surface, slanted into a cup holder. The vehicle may drive on a non-horizontal, sloped surface; it may not go straight up or down the slope (e.g., slanted parking spaces). Furthermore, unpredictable human or road condition disturbances (e.g., moved together with the driver's pants' pockets, or picked up from a cupholder; speed bumps or jerky driving jolting the phone) may change the phone pose frequently. Despite all these different scenarios and disturbances, the phone's pose must be reliably and quickly estimated.

Second, due to the lack of periodic acceleration patterns like a person's walking [6]–[8], the traveling distance of a vehicle cannot be easily estimated. Although landmarks (e.g., speed bumps, turns) causing unique inertial data patterns can calibrate the location [9], distinguishing such patterns from other movements robustly (e.g., driver picking up and then laying down the phone), and recognizing them reliably despite different parking structures, vehicles and drivers, remain open questions.

Finally, we have to balance the conflict between tracking accuracy and latency. Delaying the location determination allows more time for computation and sensing, thus higher tracking accuracy. However, this delay inevitably increases tracking latency, which adversely impacts real time performance and user experience. How to develop efficient tracking algorithms to achieve both reasonable accuracy and acceptable latency, while using resources only on the phone, is another great challenge.

VeTrack consists of several components to deal with the above challenges to achieve accurate, real time tracking. First, we propose a novel *"shadow"* trajectory tracing method that greatly simplifies phone pose estimation and vehicle movements computation. It can handle slopes and slanted driving on slopes; it is highly robust to inevitable noises, and can quickly re-estimate the pose after each disturbance. We devise robust landmark detection algorithms that can reliably distinguish landmarks from disturbances (e.g., drivers picking up the phone) causing seemingly similar inertial patterns. Based on the vehicle movements and detected landmarks, we develop a highly robust yet efficient probabilistic framework to track a vehicle's location.

In summary, we make the following contributions:

- We develop a novel robust and efficient "shadow" trajectory tracing method. Unlike existing methods [10]–[12] that track the 3-axis relative angles between the phone and vehicle, it only tracks a single heading direction difference. To the best of our knowledge, it is the first that can handle slopes and slanted driving on slopes, and re-estimates a changed pose almost instantaneously.
- We design states and algorithms in a Sequential Monte Carlo framework that leverages constraints from garage maps and detected landmarks to reliably infer a vehicle's location. It uses probability distributions to represent a vehicle's states. We further propose a one-dimensional *road skeleton* model to reduce the vehicle state complexity, and a prediction-rollback mechanism to cut down tracking latency, both by one order of magnitude to enable real time tracking.
- We propose robust landmark detection algorithms to recognize commonly encountered landmarks. They can reliably distinguish true landmarks from disturbances that exhibit similar inertial data patterns.
- We implement a prototype and conduct extensive experiments with different parking structures, vehicles and drivers. We find that it can track the vehicle in real time against even disturbances such as drivers picking up the phone. It has almost negligible tracking latency, 10° pose and $2 \sim 4$ parking spaces' location errors at the 80^{th} percentile, which are sufficient for most real time driving and parked vehicle finding.

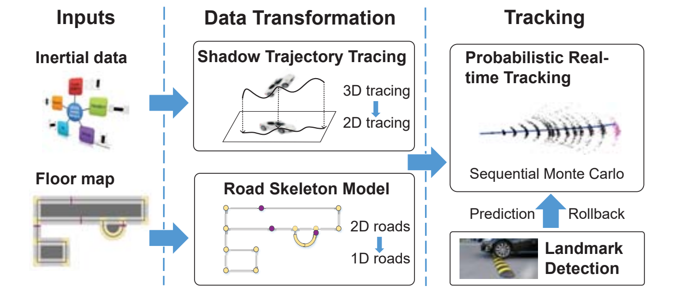

Fig. 1. In data transformation stage, the shadow trajectory tracing simplifies 3D vehicle tracing into 2D shadow tracing while road skeleton model further reduces 2D tracing into 1D. In tracking stage, VeTrack represents vehicle states probabilistically and uses a Sequential Monte Carlo framework for robust tracking. It also uses landmark detection to calibrate vehicle states and prediction/rollback for minimum latency.

Next, we give a brief overview (Section 2), describe the shadow trajectory tracing (Section 3), Sequential Monte Carlo algorithm design and the simplified road skeleton model (Section 4), landmark detection algorithms and prediction-rollback (Section 5). We report evaluation (Section 6), review related work (Section 7). After a discussion of limitations (Section **??**), we conclude the paper.

2 Design Overview

VeTrack utilizes smartphone inertial data and garage floor maps (assumed already available) as inputs, and simplifies the 3D vehicle tracing problem in the data transformation stage (Figure 1). It leverages the probabilistic framework with landmark detection results and prediction/rollback mechanism for robust and real time tracking.

The data transformation stage contains two components, i.e., shadow trajectory tracing and road skeleton model. Shadow trajectory tracing tracks the vehicle's shadow's movements on 2D plane instead of the vehicle in 3D space; the road skeleton model abstracts 2D strip roads into 1D line segments to remove inconsequential details while keeping the basic shape and topology. They together simplify the 3D vehicle tracing problem into 1D.

To deal with noises and disturbances in data, VeTrack explicitly represents the states of vehicles (e.g., locations) with probabilities and we develop algorithms in a Sequential Monte Carlo framework for robust tracking. We also leverage landmark detection results to help calibrate the vehicle locations to where such landmarks exist, and the prediction/rollback mechanism to generate instantaneous landmark recognition results while the vehicle has only partially passed landmarks.

3 Trajectory Tracing

3.1 Conventional Approaches

Inferring a vehicle's location via smartphone inertial sensors is not trivial. Naive methods such as double integration of

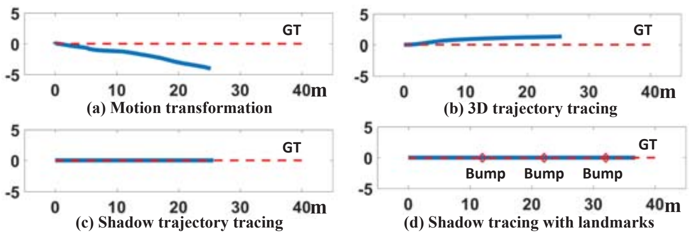

Fig. 2. Illustration of vehicle tracing using different methods: (a) motion transformation; (b) 3D trajectory tracing with gyroscope; (c) shadow trajectory tracing; (d) shadow trajectory tracing with landmarks.

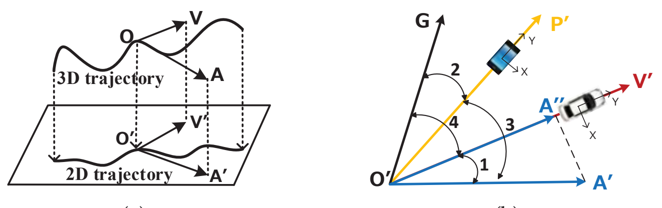

(a) (b)

Fig. 3. (a) Intuition: points O and O' are the positions of vehicle and its shadow. $\overrightarrow{OV}$ and $\overrightarrow{OA}$ are the velocity and acceleration of vehicle in the 3D space. V' and A' are the projection of V and A onto the 2D ground. (b) Illustration of the method to estimate $\angle 1$ from $\angle 2$, $\angle 3$ and $\angle 4$.

3D accelerations ($\overrightarrow{x}(t) = \iint \overrightarrow{a}(t)dt$) generate chaotic 3D trajectories due to the noisy inertial sensors. Below we list two conventional approaches.

Method 1: motion transformation. It is a straight forward approach that transforms the motion information (i.e., acceleration and orientation) from a phone to a vehicle, and eventually to that in the global 2D coordinate system. This requires the vehicle's acceleration in the global coordinate system G be estimated. After measuring the phone's acceleration from inertial sensors, existing work [10]–[12] usually take a three-step approach to transform it into vehicle's acceleration.

Assume the 3 axes of the vehicle's coordinate system are X^V, Y^V and Z^V. First the gravity direction is obtained using mobile OS APIs [13] that use low-pass Butterworth filters to remove high frequency components caused by rotation and translation movements [14]. It is assumed to be the direction of Z^V in the phone's coordinate system (i.e., vehicles moving on level ground).

Next the gravity direction component is deducted to obtain the acceleration on the horizontal plane. The direction of maximum acceleration (caused by vehicle accelerating or decelerating) is estimated as Y^V (i.e., forward direction). Finally, X^V is determined as the cross product of Y^V and Z^V using the right-hand rule. The X^V, Y^V and Z^V directions in the phone's coordinate system give a transformation matrix that converts the phone's acceleration into that of the vehicle.

Figure 2(a) shows the result of tracing a vehicle on a straight road via motion transformation. During investigation we find several limitations. First, when a vehicle is on a slope (straight up/down or slanted), the direction of gravity is no longer the Z-axis of the vehicle. Second, accelerometers are highly noisy and susceptible to various disturbances from driving dynamics and road conditions. Thus the direction of the maximum horizontal acceleration may not always be the Y-axis. In experiments we find that it has around 40^o errors at the 80^{th} percentile (Section 6.2). Finally, to reliably detect the direction of maximum horizontal acceleration, a changed phone pose must remain the same at least 4s [12], which may be impossible when frequent disturbances exist.

Method 2: 3D trajectory tracing. Instead of direct double integrating on the original acceleration vector ($\overrightarrow{x}(t) = \iint \overrightarrow{a}(t)dt$), it uses the moving direction of the vehicle (unit length vector $\overrightarrow{T}(t)$) and its speed amplitude $s(t)$: $\overrightarrow{x}(t) = \int \overrightarrow{T}(t) \cdot s(t)dt$, where $s(t)$ can be computed as $\int a(t)dt$, integration of the acceleration amplitude along moving direction. Although there are still two integrations, the impact of vertical direction noises is eliminated due to the projection, and the moving direction $\overrightarrow{T}(t)$ can be measured reliably by gyroscope.

Figure 2(b) shows the result for 3D trajectory tracing. We observe that it obtains better orientation accuracy than motion transformation, i.e., 3^o errors of the example trace, but it assumes fixed phone pose in car. In addition, raw gyroscope readings suffer linear drifts [14], and reach 32^o angle errors after an 8-minute driving in our measurements.

3.2 Shadow Trajectory Tracing

To overcome the above limitations, we propose a "shadow" trajectory tracing method that traces the movement of the vehicle's *shadow* projected onto the 2D horizontal plane (Figure 3(a)). Points O and O' represent the positions of the vehicle and its shadow. $\overrightarrow{OV}$ and $\overrightarrow{OA}$ are the velocity and acceleration of the vehicle in 3D space. V' and A' are the projection of V and A onto the 2D ground. It can be shown easily that $\overrightarrow{O'V'}$ and $\overrightarrow{O'A'}$ are the velocity and acceleration of the shadow. This is simply because the projection eliminates the vertical direction component but preserves those on the horizontal plane, thus the shadow and vehicle have the same horizontal acceleration, and thus the same 2D plane velocity and coordinates.

Shadow tracing algorithm: We need to estimate three variables in this method (Figure 3(b)): 1) the shadow's moving direction $\overrightarrow{O'V'}$ (i.e., $\overrightarrow{T}(t)$) in the global coordinate system. 2) the horizontal (i.e., shadow's) acceleration $\overrightarrow{O'A'}$. 3) angle $\angle V'O'A'$ ($\angle 1$), the angle between the horizontal acceleration vector and vehicle's shadow's heading (i.e., moving) direction; this is used to project the shadow's acceleration along the vehicle moving direction $\overrightarrow{O'V'}$ to get tangential acceleration amplitude $|\overrightarrow{O'A''}|$(i.e., $s(t)$).

Next we explain how to estimate them in three steps.

1) When the vehicle is driving straight, the shadow's moving direction is approximated by the direction of the road, which can be obtained from the garage map and the current location estimation. When the vehicle is turning around a corner, VeTrack accumulates the gyroscope's "yaw" (around gravity direction) to modify the heading direction until the vehicle goes straight again. We develop robust algorithms to distinguish straight driving from turning and disturbances (Section 5).

2) From existing mobile OS APIs [13], the gravity direction can be detected. We deduct the gravity direction component from the phone's acceleration vector to obtain the horizontal acceleration vector $\overrightarrow{O'A'}$.

3) Figure 3(b) illustrates how to calculate $\angle 1$ ($\angle V'O'A'$): $\angle 1 = \angle 2 + \angle 3 - \angle 4$ (i.e.,$\angle V'O'A' = \angle GO'P' + \angle P'O'A' - \angle GO'V'$). $\overrightarrow{O'G}, \overrightarrow{O'P'}, \overrightarrow{O'V'}$ are the Y-axes of the global, phone's shadow's and vehicle's shadow's coordinate system. 3.1) $\angle 2$ is the phone's shadow's heading direction in the global coordinate system. Its relative changes can be obtained reliably from the gyroscope's "yaw", and we use a distribution around the compass' reading upon entering the garage to initialize it. Because the Sequential Monte Carlo framework can calibrate and quickly reduce the error (Section 4), an accurate initial direction is not necessary. 3.2) $\angle 3$ is essentially the horizontal acceleration direction in the phone's shadow's coordinate system, which is already obtained in step 2). 3.3) $\angle 4$ is the vehicle's shadow's moving direction in the global coordinate system, already obtained in step 1).

Observation: Figure 2(c) shows the result for shadow trajectory tracing. We observe that the vehicle's moving direction is measured reliably by the map (i.e., forward/backward along pathways only) while phone's short-time movement in car is monitored by gyroscope, thus our method achieves better angle accuracy and robustness than the conventional approaches. However, vehicle's distance error is still larger than $14m$ due to noisy accelerometer on smartphone, thus we identify landmarks (three bumps in Figure 2(d)) to calibrate the vehicle's position. From the combination of shadow tracing and landmark calibration, the vehicle's position error is $3m$ with no angle error.

3.3 Equivalence Proof

Here we regard the 3D trajectory tracing method as the baseline, and prove that our shadow trajectory tracing method is equivalent to it in most cases and with only a small bounded difference in other cases. Note that the theoretical model and proof provide more confidence about the applicability of our approach, and a way to validate if it can be applied in certain environments.

Modeling. We denote the notations as follows. Assume P, V are the phone's, vehicle's local coordinate systems, G the global one. When used as superscripts, they denote in which coordinate system a variable is defined. V' is the vehicle's local coordinate system V rotated such that the XY-plane become horizontal[1], and the 3×3 transformation matrix from coordinate system C_1 to C_2 as $\boldsymbol{R}_{C_1}^{C_2}$. Also, two projection matrices will be used, $\boldsymbol{E}_1 = \mathrm{diag}([0,1,1])$ and $\boldsymbol{E}_3 = \mathrm{diag}([1,1,0])$ where $\mathrm{diag}(\cdot)$ represents a diagonal square matrix with the specified elements on the diagonal.

1) Baseline: 3D trajectory tracing. First we convert the phone's acceleration in its coordinate system P into that in the vehicle's coordinate system V, i.e. $a_0^P \rightarrow a_0^V$ (shown on the left part in Figure 4), then extract the tangential acceleration (i.e., acceleration along the vehicle's instantaneous moving direction) which will be transformed into the global coordinate system and integrated over time for speed and thus 3D trajectory. The pipeline of 3D trajectory tracing method has 4 stages:

1) $\boldsymbol{a}_0^P$, phone's acceleration in P.
2) $\boldsymbol{a}_0^V = \boldsymbol{R}_P^V \boldsymbol{a}_0^P$, vehicle's acceleration in V.

1. This is done by pitching X-axis horizontal then Y-axis horizontal.

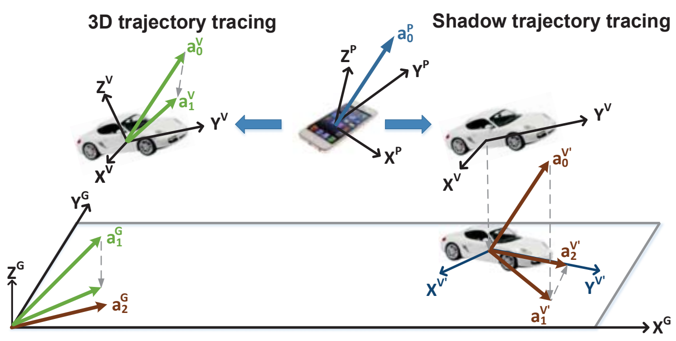

Fig. 4. Illustration of 3D trajectory tracing and shadow trajectory tracing. Left part: 3D trajectory tracing, $\boldsymbol{a}_0^P \rightarrow \boldsymbol{a}_0^V \rightarrow \boldsymbol{a}_1^V \rightarrow \boldsymbol{a}_1^G$; right part: shadow trajectory tracing, $\boldsymbol{a}_0^P \rightarrow \boldsymbol{a}_0^{V'} \rightarrow \boldsymbol{a}_1^{V'} \rightarrow \boldsymbol{a}_2^{V'} \rightarrow \boldsymbol{a}_2^G$.

3) $\boldsymbol{a}_1^V = \boldsymbol{E}_1 \boldsymbol{a}_0^V$, vehicle's tangential acceleration after eliminating radial acceleration.
4) $\boldsymbol{a}_1^G = \boldsymbol{R}_V^G \boldsymbol{a}_1^V$, vehicle's tangential acceleration in G.

Let $\Gamma(t)$ denotes the projection of vehicle's tangential acceleration on horizontal plane at time t, which can be represented as:

$$\Gamma(t) = \boldsymbol{E}_3 \boldsymbol{R}_V^G(t) \boldsymbol{E}_1 \boldsymbol{R}_P^V(t) \boldsymbol{a}_0^P(t) \tag{1}$$

where $\boldsymbol{E}_3$ is the projection.

2) Our shadow trajectory tracing method simply tracks the vehicle's shadow on horizontal plane, and its process has 5 steps (shown on the right part in Figure 4):

1) $\boldsymbol{a}_0^P$, phone's acceleration in P.
2) $\boldsymbol{a}_0^{V'} = \boldsymbol{R}_P^{V'} \boldsymbol{a}_0^P$, vehicle shadow's acceleration in V'.
3) $\boldsymbol{a}_1^{V'} = \boldsymbol{E}_3 \boldsymbol{a}_0^{V'}$, vehicle shadow's horizontal acceleration in V'.
4) $\boldsymbol{a}_2^{V'} = \boldsymbol{E}_1 \boldsymbol{a}_1^{V'}$, vehicle shadow's tangential acceleration in V'.
5) $\boldsymbol{a}_2^G = \boldsymbol{R}_{V'}^G \boldsymbol{a}_2^{V'}$, vehicle shadow's tangential acceleration in G.

Similarly, we denote $\Delta(t)$ as the shadow's tangential acceleration on horizontal plane, which is computed as:

$$\Delta(t) = \boldsymbol{R}_{V'}^G(t) \boldsymbol{E}_1 \boldsymbol{E}_3 \boldsymbol{R}_P^{V'}(t) \boldsymbol{a}_0^P(t) \tag{2}$$

Theorem: The baseline 3D trajectory tracing method and our shadow trajectory tracing method are equivalent when the X-axis or Y-axis of the vehicle (X^V or Y^V) is horizontal. Otherwise their tangential accelerations' difference is bounded by vehicle's radial acceleration times $\frac{sin^2\phi}{1+cos\phi}$, i.e.,

$$|\Gamma(t) - \Delta(t)| \leq \frac{sin^2\phi}{1+cos\phi} \cdot |\boldsymbol{a}_0^v - \boldsymbol{a}_1^v|,$$

where ϕ is the inclination angle of the slope.

We prove some Lemmas before proving the Theorem.

Lemma 1. *$\boldsymbol{E}_1$ and $\boldsymbol{E}_3$ are commutable.*

Proof. Diagonal matrices are commutable. □

Lemma 2. *$\boldsymbol{E}_3$ is commutable with $\boldsymbol{R}_{V'}^G(t)$.*

Proof. $\boldsymbol{R}_{V'}^G(t)$ is degenerated rotation along the Z-axis (Z^G and $Z^{V'}$). Thus it is commutable with $\boldsymbol{E}_3$ which eliminates the Z-axis component. □

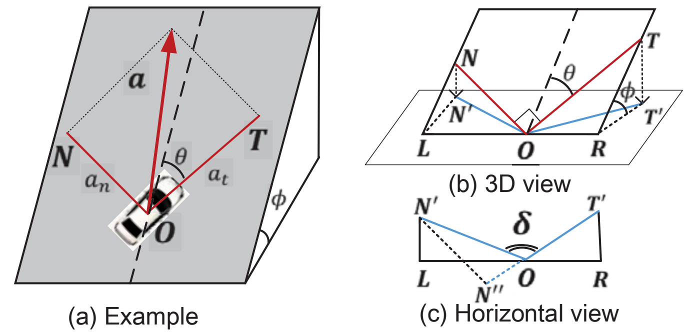

Fig. 5. (a) Driving a vehicle O on the slope with acceleration $\boldsymbol{a}$; (b) 3D view, the inclination angle of slope is ϕ, and vehicle's heading direction $\overrightarrow{OT}$ is at angle θ to the direction of slope; (c) horizontal plane view.

Lemma 3. *$\boldsymbol{E}_1$ and $\boldsymbol{R}_{V'}^{V}(t)$ are commutable when the X-axis or Y-axis of the vehicle is horizontal, otherwise $|\Gamma(t) - \Delta(t)| \leq \frac{sin^2\phi}{1+cos\phi} \cdot a_n$, where ϕ is the inclination angle of the slope and a_n is the vehicle's radial acceleration.*

Proof. As shown in Figure 5(a), we assume the vehicle O is moving on a slope (tangent plane) with inclination angle of ϕ, and its heading direction at angle θ to the direction of slope. $\boldsymbol{a} = (a_t, a_n) = (|\overrightarrow{OT}|, |\overrightarrow{ON}|)$ are the vehicle's tangential and radial accelerations.

Next, we build the spatial and plane geometry models for the two tracing methods (shown in Figure 5(b)(c)). In 3D trajectory tracing, the vehicle's tangential acceleration on horizontal plane is calculated as $\overrightarrow{OT'}$; while in shadow trajectory tracing, it is computed as $\overrightarrow{OT'} + \overrightarrow{ON''}$ where N'' denotes the projection of N' onto line $\overrightarrow{OT'}$ (the direction of vehicle's shadow). The cause of their difference $\overrightarrow{ON''}$, is that the projection of a right angle ($\angle TON$) onto horizontal ground is no longer a right angle ($\angle T'ON' = \delta$), thus vehicle's radial acceleration $\overrightarrow{ON}$ also produces horizontal acceleration component.

Then we compute their difference value $\overrightarrow{ON''}$. From Figure 5(b), we count that $|OL| = a_n \cos\theta$, $|OR| = a_t \sin\theta$, $|LN'| = a_n \sin\theta \cos\phi$, $|RT'| = a_t \cos\theta \cos\phi$. Thus $\overrightarrow{ON''}$ in Figure 5(c) can be computed via the cosine theorem:

$$\overrightarrow{ON''} = |ON'| \cos\delta = \frac{-a_n \sin\theta \sin^2\phi}{\sqrt{\cos^2\phi + \tan^2\theta}} \tag{3}$$

From Equation 3, we observe that the difference between two tracing methods does not rely on the vehicle's tangential acceleration, and they have no differences when the vehicle drives on horizontal plane ($\phi = 0°$), or either of X, Y-axis of the vehicle is horizontal ($\theta = 0°$ or $90°$).

Furthermore, we leverage algebraic formulas to compute the maximum value of $|\overrightarrow{ON''}|$, i.e., the bound of difference between two tracing methods. Given a fixed slope with inclination angle of ϕ, the maximum value of $|\overrightarrow{ON''}|$ is computed as:

$$|\overrightarrow{ON''}| = \frac{a_n \sin^2\phi}{\sqrt{\frac{\cos^2\phi}{\sin^2\theta} + \frac{1}{\cos^2\theta}}} \leq \frac{\sin^2\phi}{1+\cos\phi} \cdot a_n \tag{4}$$

and its maximum value is obtained when $\theta = \arcsin\sqrt{\frac{\cos\phi}{1+\cos\phi}}$.

Thus when the X-axis or Y-axis of the vehicle is horizontal, two tracing methods are equivalent and $\boldsymbol{R}_{V'}^{V}(\tau)$ is degenerated rotation along X-axis or Y-axis thus commutable with matrice $\boldsymbol{E}_1$, which is similar to the case in Lemma 2.

Otherwise, those two matrices are not commutable since projections of two perpendicular lines to horizontal plane is no longer perpendicular. However, the difference is bounded based on the inclination angle of the slope. Most garage paths have small degrees of slope, if any. For example, for 10° and 20° slopes, the difference between two tracing methods is less than 2% and 7% of vehicle's radial acceleration, respectively. □

Now we prove the Theorem, i.e., the equivalence between $\Gamma(t)$ in 3D trajectory tracing and $\Delta(t)$ in shadow trajectory tracing when X-axis or Y-axis of the vehicle is horizontal.

Proof. When X-axis or Y-axis of the vehicle is horizontal,

$$\begin{aligned}
\Delta(t) &= \boldsymbol{R}_{V'}^{G}(t)\boldsymbol{E}_1\boldsymbol{E}_3\boldsymbol{R}_{P}^{V'}(t)\boldsymbol{a}_0^{P}(t)(\text{Equation 2}) \\
&= \boldsymbol{R}_{V'}^{G}(t)\boldsymbol{E}_3\boldsymbol{E}_1\boldsymbol{R}_{P}^{V'}(t)\boldsymbol{a}_0^{P}(t)(\text{Lemma 1}) \\
&= \boldsymbol{E}_3\boldsymbol{R}_{V'}^{G}(t)\boldsymbol{E}_1\boldsymbol{R}_{P}^{V'}(t)\boldsymbol{a}_0^{P}(t)(\text{Lemma 2}) \\
&= \boldsymbol{E}_3\boldsymbol{R}_{V}^{G}(t)\boldsymbol{R}_{V'}^{V}(t)\boldsymbol{E}_1\boldsymbol{R}_{P}^{V'}(t)\boldsymbol{a}_0^{P}(t) \\
&= \boldsymbol{E}_3\boldsymbol{R}_{V}^{G}(t)\boldsymbol{E}_1\boldsymbol{R}_{V'}^{V}(t)\boldsymbol{R}_{P}^{V'}(t)\boldsymbol{a}_0^{P}(t)(\text{Lemma 3}) \\
&= \boldsymbol{E}_3\boldsymbol{R}_{V}^{G}(t)\boldsymbol{E}_1\boldsymbol{R}_{P}^{V}(t)\boldsymbol{a}_0^{P}(t) = \Gamma(t)(\text{Equation 1})
\end{aligned} \tag{5}$$

Thus $\Gamma(t)$ in 3D trajectory tracing and $\Delta(t)$ in shadow trajectory tracing are equivalent in this case. □

Comparison: Despite their equivalence in most cases, shadow tracing needs much less variables and is subject to less noises, thus more robust than 3D tracing. 1) Shadow tracing does not need to track variables in the vertical dimension (e.g., altitude, angle, speed and acceleration). All of them are subject to noises and require more complexity to estimate. 2) On the horizontal plane, the moving direction can be estimated accurately based on the prior knowledge of road directions (Section 4.4). The distance is computed using the acceleration amplitude along the moving direction. Thus inertial noises perpendicular to the moving direction do not impact the distance estimation. 3) Shadow tracing uses gyroscopes to estimate pose, while conventional approaches use accelerometers that are more susceptible to external disturbances. Therefore, shadow tracing is much less complex, subject to less noises, and thus achieves better accuracy and higher robustness.

During experiments, we find that: our shadow tracing method can handle arbitrary phone and vehicle poses and the vehicle can go straight up/down or slanted on a slope. It has much smaller errors ($5 \sim 10°$ at the 80th percentile) and better robustness. It also re-estimates a changed phone pose almost instantaneously because gyroscopes have little latency; thus it can handle frequent disturbances.

4 Real Time Tracking

4.1 Intuition

The basic idea to locate the vehicle is to leverage two types of constraints imposed by the map, namely paths and landmarks. Given a trajectory estimated from inertial data

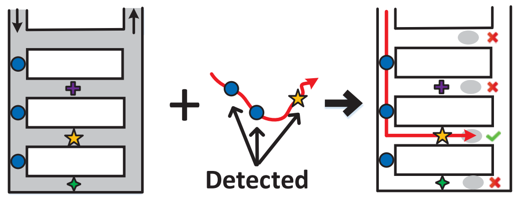

Fig. 6. Using both map constraints and detected landmarks can narrow down the possible placement of the trajectory more quickly.

(Figure 6), there are only a few paths on the map that can accommodate the trajectory. Each detected landmark (e.g., a speed bump or turn) can pinpoint the vehicle to a few possible locations. Jointly considering the two constraints can further reduce the uncertainty and limit the possible placement of the trajectory, thus revealing the vehicle location. We will first describe the tracking design here, then landmark detection in Section 5.

To achieve robust and real time tracking, we need to address a dual challenge. First, the inertial data have significant noises and disturbances. Smartphones do not possess a speedometer or odometer to directly measure the velocity or distance; they are obtained from acceleration integration, which is known to generate cubic error accumulation [9]. External disturbances (e.g., hand-held movements or road conditions) cause sudden and drastic changes to vehicle movements. Together they make it impossible to obtain accurate trajectories from inertial data only. Second, the requirement of low latency tracking demands efficient algorithms that can run on resource-limited phones. We have to minimize computational complexity so no cloud backend is needed.

To achieve robustness, we use probability distributions to explicitly represent vehicle states (e.g., location and speed) and the Sequential Monte Carlo (SMC) method to maintain the states. This is inspired by probabilistic robotics [15]: instead of a single "best guess", the probability distributions cover the whole space of possible hypotheses about vehicle locations, and use evidences from sensing data to validate the likelihoods of these hypotheses. This results in much better robustness to noises in data. To achieve efficiency, we use a 1D *"road skeleton"* model that abstracts paths into one dimensional line segments. We find this dramatically reduces the size of vehicle states. Thus the number of hypotheses is cut by almost one order of magnitude, which is critical to achieve real time tracking on resource limited phones. Next we will describe the road skeleton model and the detailed SMC design.

4.2 Road Skeleton Model

The road skeleton model greatly simplifies the representation of garage maps. It abstracts away inconsequential details and keeps only the essential aspects important to tracking. Thus it helps reduce computational overheads in the probabilistic framework. We assume that garage maps are available (e.g., from operators), while how to construct them is beyond the scope of this paper.

Given a map of the 3D multi-level parking structure, we represent each level by projecting its map onto a 2D horizontal plane perpendicular to the gravity direction. Thus the vehicle location can be represented by a number indicating the current level, and a 2D coordinate for its location on this level. To accommodate changes when a vehicle moves across adjacent levels, we introduce "virtual boundaries" in the middle of the ramp connecting two levels. As shown in Fig.7(b), a vehicle crossing the dash line of the virtual boundary between levels will be assigned a different level number. This kind of 2D representation suits the needs for shadow tracing while retaining the essential topology and shape for tracking.

Note that we call it 2D representation because the floor level remains unchanged and does not need detection most of the time. It is updated only when the vehicle crosses virtual boundaries between levels. Its estimation is also much simpler and easier than accurate 2D tracking, where most challenges exist.

The key insight for the skeleton model is that the road width is not necessary for tracking vehicle locations. Since the paths are usually narrow enough for only one vehicle in each direction, the vehicle location has little freedom in the width direction. Thus we simplify the road representation with their medial axis, and roads become 1D line segments without any width.

We have tried several geometrical algorithms to extract the road skeleton from garage floor map. A naive method is to extract the road boundary, then leverage Voronoi diagram [16] to generate the middle line inside the road boundary (shown in Figure 7(c)). However, we observe that there are superfluous and deformed, non-straight 1D line segments on the skeleton. Those mistakes are difficult to remove by simple geometrical algorithms.

Thus we leverage a robust thinning method [17] to extract the road skeleton (Figure 7(d)) and eliminate such problems. Then we project the bumps from garage floor map onto the road skeleton, and use a 3×3 pixel template to find road turns on the skeleton map. The final road skeleton model with landmarks are shown in Figure 7(e).

Compared to a straightforward 2D strip representation of roads, the skeleton model reduces the freedom of vehicle location by one dimension, thus greatly cutting down the state space size in the probabilistic framework and resulting in one order of magnitude less complexity.

4.3 Probabilistic Tracking Framework

The tracking problem is formulated as a Sequential Monte Carlo (SMC) problem, specifically, the particle filtering framework [15]. The vehicle states (e.g., location, speed) at time t are represented by a multi-dimensional random variable $s(t)$. Each hypothesis (with concrete values for each dimension of $s(t)$) is called a "particle" and a collection of J particles $\{s_t^{(j)}\}_{j=1}^J$ are used to represent the distribution of possible vehicle states at time t.

The framework operates on discrete time $\{1, ..., t-1, t, ...\}$ and repeats three steps for each time slot. Without loss of generality, we assume J particles $\{s_{t-1}^{(j)}\}_{j=1}^J$ already exist at $t-1$ and describe the progress from $t-1$ to t.

State update predicts the set of states $\{\hat{s}_t^{(j)}\}_{j=1}^J$ at time t based on two known inputs, the previous state $\{s_{t-1}^{(j)}\}_{j=1}^J$ and most recent movement m_t such as the speed, acceleration that govern the movement of the vehicle. For example,

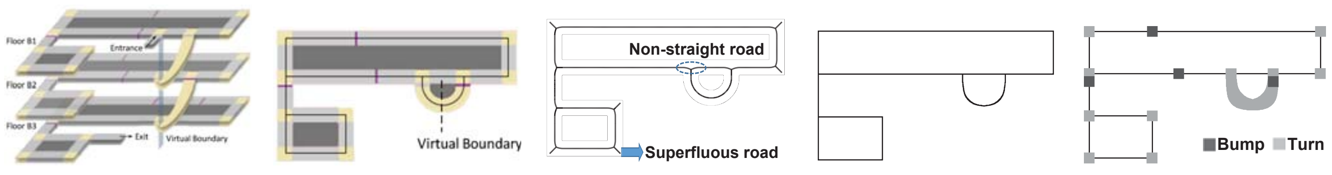

(a) 3D floor plan (b) 2D floor plan (c) Voronoi diagram (d) Thinning method (e) Road skeleton model

Fig. 7. (a) shows the 3D floor plans of a multi-level parking structure. A vehicle enters the entrance on the floor B1, goes down to other two levels crossing the virtual boundaries. (b) shows the 2D projection of Floor B2 in (a). (c) shows the road skeleton via Voronoi diagram, and there are superfluous and non-straight 1D lines. (d) shows the road skeleton via a robust thinning method. (e) shows the final 1D road skeleton model, with points representing landmarks (corresponding to bumps and turns).

given the previous location and most recent speed, one can predict a vehicle's next location. To capture uncertainties in movement and previous states, a random noise is added to the estimated location. Thus J predictions $\{\hat{s}_t^{(j)}\}_{j=1}^J$ are generated.

Weight update uses measurements z_t made at time t to examine how much evidence exists for each prediction, so as to adjust the weights of particles $\{\hat{s}_t^{(j)}\}_{j=1}^J$. The likelihood $p(z_t|s_t)$, how likely the measurement z_t would happen given state s_t, is the evidence. A prediction $\hat{s}_t^{(j)}$ with a higher likelihood $p(z_t|s_t = \hat{s}_t^{(j)})$ will receive a proportionally higher weight $w_t^{(j)} = w_{t-1}^{(j)} p(z_t|s_t = \hat{s}_t^{(j)})$. Then all weights are normalized to ensure that $\{w_t^{(j)}\}_{j=1}^J$ sum to 1.

Resampling draws J particles from the current state prediction set $\{\hat{s}_t^{(j)}\}_{j=1}^J$ with probabilities proportional to their weights $\{w_t^{(j)}\}_{j=1}^J$, thus creating the new state set $\{s_t^{(j)}\}_{j=1}^J$ to replace the old set $\{s_{t-1}^{(j)}\}_{j=1}^J$. Then the next iteration starts.

Note that the above is only a framework. The critical task is the detailed design of particle states, update, resampling procedures. Thus we cannot simply copy what has been done in related work, and have to carefully design algorithms tailored to our specific problem.

4.4 Tracking Algorithms

4.4.1 State and Initialization

Our particle state is a collection of factors that can impact the vehicle tracking. Since the number of particles grows exponentially with the dimensionality of the state, we select most related factors to reduce the complexity while still preserving tracking accuracy. Our particle states include:

- level number k,
- position on 2D floor plane $X = (x, y)$,
- speed of the vehicle v,
- α/β, phone/vehicle shadows' 2D heading directions.

The first dimension k is introduced for multi-level structures. Position of the vehicle is represented as a 2D coordinate $X = (x, y)$ for convenience. In reality, due to the 1D skeleton road model, the position actually has only one degree of freedom. This greatly reduces the number of particles needed.

Initialization of particles: We use certain prior knowledge to initialize the particles' state. The last GPS location before entering the parking structure is used to infer the entrance, thus the level number k and 2D entrance location (x, y). The vehicle speed v is assumed to start from zero. The vehicle heading direction β is approximated by the direction of the entrance path segment, and the phone heading direction α is drawn from a distribution based on the compass reading before entering the garage. As shown later (Section 6), the phone's heading direction can be calibrated to within $15°$, showing strong robustness against compass errors known to be non-trivial [18].

4.4.2 State Update

For a particle with state $(k_{t-1}, x_{t-1}, y_{t-1}, v_{t-1}, \alpha_{t-1}, \beta_{t-1})$, we create a prediction $(\hat{k_t}, \hat{x_t}, \hat{y_t}, \hat{v_t}, \hat{\alpha_t}, \hat{\beta_t})$ given movement $m_t = (a_x, a_y, \omega_z)$ where a_x, a_y and ω_z are X, Y-axis accelerations and Z-axis angular speed in the coordinate system of the phone's shadow.

First, $(\hat{x_t}, \hat{y_t})$ is updated as follow:

$$\hat{x_t} = x_{t-1} + v_{t-1}\Delta t \cdot \cos\beta_{t-1} + \epsilon_x, \tag{6}$$

$$\hat{y_t} = y_{t-1} + v_{t-1}\Delta t \cdot \sin\beta_{t-1} + \epsilon_y, \tag{7}$$

where ϵ_x, ϵ_y are Gaussian noises. If $(\hat{x_t}, \hat{y_t})$ is no longer on the skeleton, we project it back to the skeleton. Level number $\hat{k_t}$ is updated when a particle passes through a virtual boundary around the floor-connecting-ramp, otherwise $\hat{k_t} = k_{t-1}$.

Next, velocity v_t is updated as follow:

$$\hat{a_t} = a_y \cdot \cos\gamma_t - a_x \cdot \sin\gamma_t + \epsilon_a, \tag{8}$$

$$\hat{v_t} = v_{t-1} + a_t \cdot \Delta t + \epsilon_v, \tag{9}$$

where γ_t is the angle between the Y axes of the two shadows' coordinate systems and ϵ_a, ϵ_v are Gaussian noises.

Finally, α_t and β_t are updated as follows:

$$\hat{\alpha_t} = \alpha_{t-1} + \omega_z \Delta t + \epsilon_\alpha, \tag{10}$$

$$\hat{\beta_t} = \begin{cases} \beta_{t-1} + \omega_z \Delta t + \epsilon_\beta, & \text{if } turn = True; \\ \text{road direction at } (k_t, x_t, y_t), & \text{otherwise.} \end{cases} \tag{11}$$

where $\epsilon_\alpha, \epsilon_\beta$ are random Gaussian noises. The above allows the phone to change its angle α to accommodate occasional hand-held or jolting movements, while such movements will not alter the vehicle's angle β if the vehicle is known to travel straight.

4.4.3 Weight Update

Weight update uses detected landmarks and floor plan constraints to recalculate the "importance" of the current particle states. The basic idea is to penalize particles that behave inconsistently given the floor plan constraints. For example, since a vehicle cannot travel perpendicularly to path direction, a particle with velocity orthogonal to the road direction will be penalized. It will have much smaller weights and less likely to be drawn during resampling.

We compute the weight w_t as

$$w_t := w_{t-1} \prod_{i=0}^{2} w_{ti}, \tag{12}$$

Each w_{ti} is described as follows.

- **Constraints imposed by the map.** We define $w_{t0} = \cos^2(\beta_t - \beta_{t-1})$. It is designed to penalize particles that have a drastic change in the vehicle heading direction, since during most of the time a vehicle does not make dramatic turns.
- **Detected landmarks.** When an i-th type landmark [2] is detected, w_{ti} of the current state is updated as $\mathcal{N}(D_i(x_t, y_t); 0, \sigma_i^2)$ where $D_i(x_t, y_t)$ is the distance to the closest landmark of the same type and σ_i^2 is a parameter controlling the scale of the distance. If no landmark is detected, $w_{ti} = 1$. This method penalizes the predicted states far away from detected landmarks.

Finally all weights are normalized so they sum up to 1.

4.4.4 Resampling

A replacement particle is selected from the predicted particle set $\{\hat{s}_t^{(j)}\}_{j=1}^J$ where each particle $\hat{s}_t^{(j)}$ has probability $w_t^{(j)}$ being selected. This is repeated for J times and J particles are selected to form the new state set $\{s_t^{(j)}\}_{j=1}^J$. Then the next iteration starts.

5 Landmark Detection

A parking structure usually has a limited number of landmarks (e.g., speed bumps and turns), and their locations can be marked on the garage map. When a vehicle passes over a landmark, it causes distinctive inertial data patterns, which can be recognized to calibrate the vehicle's location.

However, realizing accurate and realtime landmark detection is not trivial because: 1) road conditions and hand movements impose disturbances on inertial sensor readings; and 2) to minimize delay, landmark recognition results are needed based on partial data before the vehicle completely passes a landmark. We present landmark detection algorithms robust to noises and hand movements, and a prediction and rollback mechanism for instantaneous landmark detection.

5.1 Types of Landmarks

Speed bumps generate jolts, hence acceleration fluctuations in the Z-axis when a vehicle passes over. Note that drainage trench covers, fire shutter bottom supports may also cause similar jolting patterns. We include them as "bumps" as well in the garage map.

Many factors can cause ambiguities in bump detection. For example, Figure 8 shows the acceleration signal along the Z-axis as a vehicle starts and passes over four bumps

2. We use only bump and corner here because their locations are precise; turns are used in vehicle angle β update in Eqn 11.

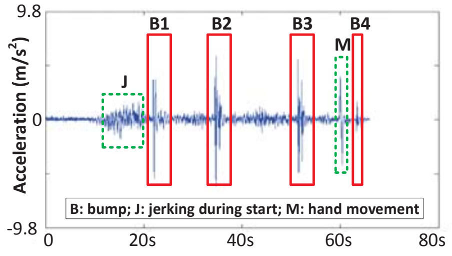

Fig. 8. Acceleration along the Z-axis. There are starting acceleration (J), four bumps (B1-B4) and one hand movement (M) along the trajectory.

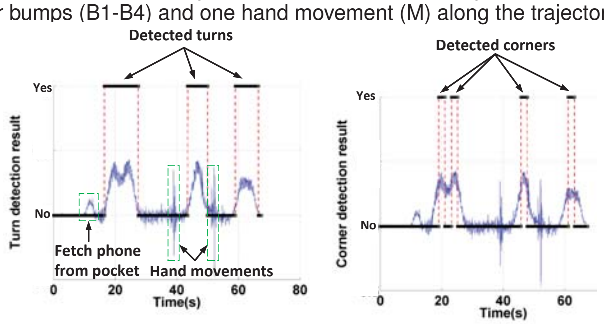

(a) Turn detection (b) Corner detection

Fig. 9. Turn and corner detection. (a) Three turn periods are correctly detected, even there are several different hand movements. (b) 4 corners are correctly separated, even when only 3 turned are detected.

along a straight road. The first tremor in the left green box (around $10 \sim 17s$ marked with "J") is caused by the vehicle's starting acceleration. It lasts longer but with smaller magnitude compared to those caused by the bumps (in red boxes marked "$B1$"-"$B4$"). The tremor in the right green box (around 60s marked "M") is due to the user's action - holding the phone in hand, then uplifting the phone to check the location. They generate vertical acceleration that may be confused with those by bumps.

Turns are defined as durations in which a vehicle continuously changes its driving direction, usually around road corners. They can be detected from the gyroscope readings of angular velocities around the gravity direction (i.e., "yaw"). During turns a vehicle's direction differs from the road direction. Its direction changes in such periods are accumulated to track the vehicle's heading direction.

There exists work [12] using simple thresholding on turning angles to detect turns. However, we find they cannot reliably distinguish vehicle turns from hand movements (e.g., putting the phone on adjacent seat and picking it up to check the location).

Corners. A turn may span over an extended period, from its start to the end. The corner where two road segments join can be used to precisely calibrate the vehicle's location. The main challenge is consecutive turns: they might be detected as a single one, hence missing some corners. For example, in Figure 9(a), the first two turns may be detected as only one turn period.

We observe that when a vehicle passes at a corner, its angular velocity usually is at a local maxima, corresponding to the maximum turn of the steering wheel. To identify corners precisely, we use a sliding window to find local maxima of angular velocities within each turning period. Each local maxima is marked as a corner. Figure 9(b) shows that the left most two consecutive corners within the same turn period are properly separated.

5.2 Feature and Classification Algorithm

We use machine learning techniques to recognize bumps and turns. Corners are detected within turns using the above local maxima searching. The critical issue is what features should be used. Although one may feed the raw signal directly to these algorithms, it is usually much more efficient to design succinct, distinctive features from raw signals.

For bumps, we divide acceleration along the Z-axis into 2-second windows sliding at 0.2s intervals. This window size is chosen empirically such that both front and rear wheels can cross the bump for complete bump-passing. For turns, we use gyroscope angular velocities around the vertical direction, and divide the signal the same way. We observe that smaller windows lead to drastic accuracy drop, while larger ones incurs more delay.

We observe that there are two kinds of common hand movements that may be confused with bumps or turns: 1) hold the phone in hand, and occasionally uplift it to check the location; 2) put the phone in pockets/nearby seat, pick up the phone to check the location and then lay it down. The first causes a jitter in Z-axis acceleration, and might be confused with bumps; the second also has Z-axis gyroscope changes, and might be confused with turns.

We have tried a number of different feature designs, both time-domain and frequency-domain, to help distinguish such ambiguities. We list five feature sets which are found to have considerable accuracy and low computation complexity (detailed performance in Section 6).

(1) **STAT35** (35 dimensions): we equally divide one window into 5 segments, and compute a 7-dimensional feature [19] from each segment, including the mean, maximum, second maximum, minimum, and second minimum absolute values, the standard deviation and the root-mean-square.

(2) **DSTAT35** (70 dimensions): In addition to STAT35, we also generate a "differential signal" (i.e., the difference between two consecutive readings) from the raw signal, and extract a similar 7-dimensional feature from each of its 5 segments.

(3) **FFT5** (5 dimensions): we do FFT on the raw signal in the whole window, and use the coefficients of the first five harmonics as a 5-dimensional feature.

(4) **S7FFT5** (35 dimensions): in addition to FFT5, we also extract the same 5 coefficients from each of two half-size windows, and four quarter-size windows. Thus we obtain 35 dimensions from 7 windows.

(5) **DFFT5** (10 dimensions): the first five FFT coefficients of both raw and differential signals.

We explore a few most common machine learning algorithms, Logistic Regression (LR) [20] and Support Vector Machine (SVM) [20]. After feature extraction, we manually label the data for training. We find that SVM has higher accuracy with slight more complexity than LR, while both can run fast enough on the phone. So we finally decide to use SVM in experiments. We find it has bump and turn detection accuracies (percentage of correctly labeled samples) around 93% (details in Section 6.2).

We have also tried some threshold-based methods on temporal [21] and frequency domain [22] features, but find it is impossible to set universally effective thresholds, and the frequency power densities by hand movements can be very similar to those of landmarks. Thus they are not sufficiently robust.

5.3 Prediction and Rollback

The reliability of landmark detection depends on the "completeness" of the signal. If the window covers the full duration of passing a landmark, more numbers of distinctive features can be extracted, and the detection would be more reliable. In reality, this may not always be possible. The landmark detection is repeated at certain intervals, but many intervals may not be precisely aligned with complete landmark-passing durations. One naive solution is to wait until the passing has completed. Thus more features can be extracted for reliable detection. However, this inevitably increases tracking latency and causes jitters in location estimation and display, adversely impacting user experience.

We use a simple prediction technique to make decisions based on data from such partial durations. To identify whether a car is passing a landmark at time t, assume that the signal spanning from $t-\tau$ to $t+\tau$ covering the full 2τ landmark-passing duration is needed for best results. At any time t, we use data in window $[t-2\tau, t]$ to do the detection. The results are used by the real time tracking component to estimate the vehicle location. At time $t+\tau$, the data of full landmark-passing duration become available. We classify data in $[t-\tau, t+\tau]$ and verify if the prediction made at t is correct. Nothing needs to be done if it is. If it was wrong, we rollback all the states in the tracking component to t, and repeat the computation with the correct detection to re-estimate the location.

This simple technique is based on the observation that most of the time the vehicle is driving straight and landmarks are rare events. Thus the prediction remains correct most of the time (i.e., during straight driving), and mistakes/rollbacks happen only occasionally (i.e., when a landmark is encountered). From our experiments, rollbacks happen in a small fraction ($\sim$ 10%) of the time. Thus we ensure low latency most of the time because there is no waiting, while preserving detection accuracy through occasional rollback, which incurs more computation but is found to have acceptable latency ($0.05 \sim 0.2$s) (Section 6).

6 Performance Evaluation

6.1 Methodology

We implement VeTrack on iOS 6/7/8 so it can run on iPhone 4/4s/5/5s/6. Our code contains a combination of C, C++ for algorithms and Objective C for sensor and GUI operations. A sensor data collector sends continuous data to landmark detectors to produce detection results. Then the real time tracking component uses such output to estimate the vehicle's location, which is displayed on the screen. The initialization (e.g, loading map data) takes less than 0.5 second. Sensors are sampled at 50Hz and the particle states are evolved at the same intervals ($20ms$). Since each landmark lasts for many $20ms$-intervals, the detectors classify the landmark state once every 10 samples (i.e., every 0.2 second), which reduces computing burden.

We conduct experiments in three underground parking lots: a $250m \times 90m$ one in an office building, a $180m \times 50m$ one in a university campus and a 3-level $120m \times 80m$ one in

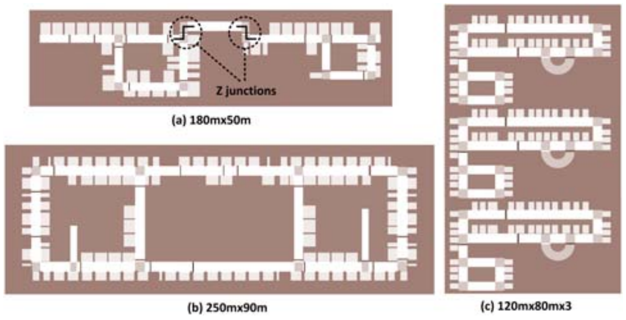

Fig. 10. Floor maps of three underground parking lots: (a) university campus: $180m \times 50m$ with 79 parking spots, 12 bumps and 11 turns. (b) office building: $250m \times 90m$ with 298 parking spots, 19 bumps and 10 turns. (c) shopping mall: 3-level $120m \times 80m$ with 423 parking spots, 10 bumps and 27 turns. The chosen parking spots and entrance are marked for each lot.

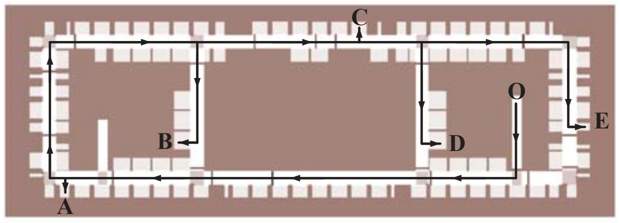

Fig. 11. Driving trajectories and test spots. Each trajectory begins at the entrance O and ends at one of the test spots (A to E).

a shopping mall. Before the experiments, we have measured and drawn their floor plans (shown in Figure 10). There are 298, 79, 423 parking spots, 19, 12, 10 bumps, 10, 11, 27 turns and 4, 2, 6 slopes, respectively.

For each parking lot, we collect 20 separate trajectories each starting from the entrance to one of the parking spots (shown in Figure 10) for inertial sensor data at different poses. The average driving time for trajectories is 2∼3 minutes, and the longest one 4.5 minutes. Exemplar trajectories to five test spots are illustrated in Figure 11.

For all three lots, we use a mould to hold 4 iPhones with 4 different poses: horizontal, lean, vertical and box (Figure 12(a)). To further test the performance and robustness of our system, we use 4 more iPhones for the challenging 3-level parking lot with one in driver's right pants' pocket, one in a bag on a seat and two held in hand. The one in pocket is subject to continuous gas/brake pedal actions by the driver, while the one in bag to vehicle movements. Once in a while, one hand-held phone is picked up and put down on the user's thigh, causing Z-axis accelerations similar to those by bumps; the other is picked up from and laid down to adjacent seat, causing Z-axis angular changes similar as those by turns. These 8 poses hopefully cover all common driving scenarios. The UI of VeTrack is shown in Figure 12(b).

We use video to obtain the ground truth of vehicle location over time. During the course of driving, one person holds an iPad parallel to the vehicle's heading direction to record videos from the passenger window. After driving, we manually examine the video frame by frame to find when the vehicle passed distinctive objects (e.g., pillars) with known locations on the map. Such frames have those objects in the middle of the image, thus the error is bounded by 0.5 vehicle length and usually much better.

To align inertial data and video collected from different

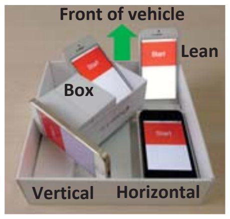

(a) Mould

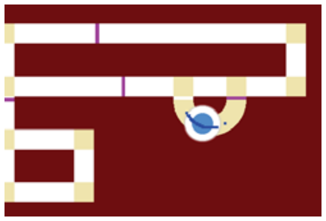

(b) VeTrack UI

Fig. 12. Mould and VeTrack UI.

devices temporally, we first synchronize the time on all the iPhones and iPad. Then different people holding different devices will start the data collecting/recording applications at the same time. These operations establish the correspondence of data in the time series of different devices.

6.2 Evaluation of Individual Components

Landmark classification accuracy. To train landmark detectors and test their performance, we use recorded videos to find encountered landmarks and label their locations on the whole trajectory. Then we use sliding windows to generate labeled segments of sensor readings. Note that disturbances caused by hand movements are labeled as non-bump and non-turn because they should not be confused with bumps or turns. In total we generate 14739 segments for bump detector and 57962 segments for turn detector.

We evaluate classification accuracy (percentage of test samples correctly classified) of six different sets of features (described in Section 5). We randomly choose 50% of the whole dataset to train the SVM classifier and others to test the performance. We repeat it 20 times and report the average performance in Table 1. It shows that they all have high accuracy around 90%. We decide to use DFFT5 with relatively high accuracies (93.0% and 92.5% for bump and turn) and low complexity in further evaluation.

TABLE 1
Accuracies of different feature sets.

	dimension	bump	turn
STAT35	35	92.7%	92.8%
DSTAT35	70	92.6%	93.4%
FFT5	5	91.8%	92.2%
S7FFT5	35	92.5%	92.6%
DFFT5 (chosen)	10	93.0%	92.5%

We repeat the test across different garages: using the data from one as training and another as testing. In reality, we can only obtain data from a limited number of garages for training, at least initially. Thus this test critically examines whether high accuracies are possible for vast numbers of unknown garages. Table 2 shows the cross-test accuracies of bump and turn detection, respectively. Each row represents training data and column test data. We observe that the accuracies are around, and some well above 90%. This encouraging evidence shows that it is very possible to retain the accuracy when training data are available from only limited numbers of garages.

Precision and recall of landmark detection.

After training landmark detectors, we further test their precision (ratio of true detections among all detected landmarks) and recall (ratio of true detections to groundtruth number of such landmarks) over whole traces. They tell how

TABLE 2
Cross-test of bump/turn detection (%)

train/test	office	campus	mall
office	95.5/93.6	91.9/95.6	90.1/90.3
campus	93.7/94.1	93.9/96.3	88.5/90.8
mall	94.1/92.3	90.6/94.6	91.5/91.0

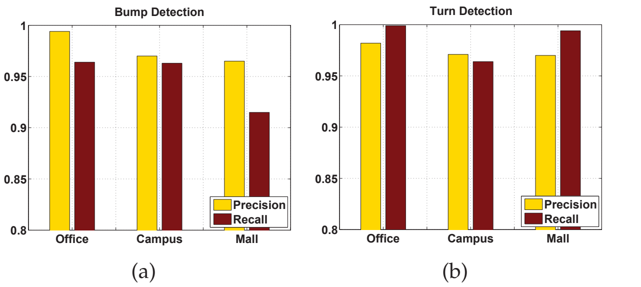

Fig. 13. Precision and recall of bump and turn detection in three different garages.

likely the detector makes mistakes (high precision means less chances for mistakes), and how close all groundtruth ones are detected (high recall means more real ones are detected). An ideal detector would have 100% precision and recall.

The precision and recall of bump and turn detection are shown in Figure 13. Both prediction and recall of bump detection are over 91% and those of turn are over 96%. Turn detection has better performance because it uses features from more reliable gyroscope data. We also find that poses in the mould has the best performance because they have the least disturbances; those in pocket and bag are better than in those in hand because they do not experience disturbances from hand movements.

Accuracy of shadow tracing. The performance of trajectory tracing highly depends on the accuracy of phone pose estimation (relative orientation between the phone and vehicle's coordinate systems). We compare its accuracy in 3D and 2D tracing methods. Similar to other work [10], [11], we use principle component analysis (PCA) in 3D method to find the maximum acceleration direction as Y-axis. To obtain the ground truth, we fix a phone to the vehicle and align its axes to those of the vehicle. The error is defined as the angle between the estimated and ground truth Y-axis of the phone. For fair comparison, we project the 3D pose to horizontal plane before calculating its error.

The CDFs of errors (Figure 14) show that: 1) Our 2D method is more accurate, with the 90^{th} percentile error at $10 \sim 15^o$ while that of the 3D method is around $50^o \sim 70^o$, which in reality would make accurate tracking impossible. 2) The 2D method is more robust to disturbances in unstable poses such as pocket/bag and hand-held, whereas the 3D method has much larger errors for the latter two. This shows that our shadow tracing is indeed much more practical for real driving conditions. In addition, we find that the PCA needs a window of 4s for unchanged pose, while the 2D method is almost instantaneous.

6.3 Realtime Tracking Latency

Realtime tracking latency is the time the tracking component needs to finish computing the location after obtaining sensor data at t. When there are prediction mistakes, it also includes latencies for detecting mistakes, rollback and

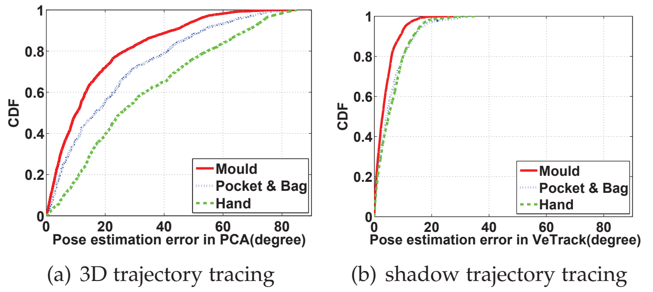

Fig. 14. CDFs of pose estimation error: (a) 3D method. (b) Our 2D method.

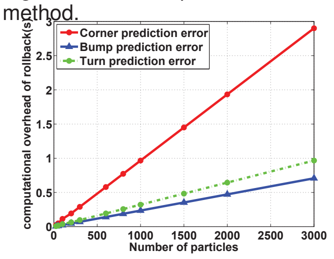

Fig. 15. Latency by different rollback types and numbers of particles.

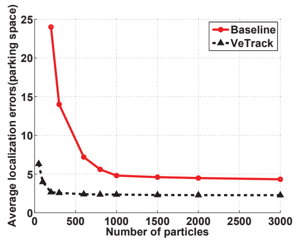

Fig. 16. Tracking error by numbers of particles.

re-computing of the current location. This is measured on iPhone 4s, a relatively slower model. As shown in Table 3, landmark detection for bump, turn and corner each cost $\sim$ 0.2ms. In almost $\sim$ 90% of time where predictions are correct, one round of tracking is computed within 1.7ms. The 2.3ms computing finishes within the 20ms particle state update interval, causing no real time delay. For about $\sim$ 10% of time, recovering for bump, turn and corner errors (each $\sim$3%) take 64ms, 47ms and 193ms. The worst case is less than $0.2s$, hardly noticeable to human users.

TABLE 3
Realtime Tracking Latency.

	bump	turn	corner
landmark detection	0.21ms	0.22ms	0.22ms
90% realtime tracking		1.7ms	
10% rollback	47ms	64ms	193ms

Figure 15 shows the latency as a function of number of particles, each curve for one different type of wrong predictions resulting in rollback. All curves grows linearly, simply because of the linear overhead to update more particles. Note that the difference between latencies of different curves is caused by different sizes of rollback windows (1s, 1s and 3s for bump, turn and corner detection errors, respectively). Although bump and turn detection have the same rollback window sizes, recovering turn errors has slightly higher computation overhead. In experiments we find that 100 $\sim$ 200 particles can already achieve high accuracy, which incurs only 0.05 $\sim$ 0.2s) latency. Such disruptions are minimal and not always perceptible by users.

6.4 Tracking Location Errors

Parking location errors. The final parking location is important because drivers use it to find the vehicle upon return. We use the number of parking spaces between the real and estimated locations as the metric, since the search effort depends more on how many vehicles to examine, not the absolute distance.

In order to compare all 8 poses, we show the results in the mall garage. Figure 17(a) shows the 4 phones in the

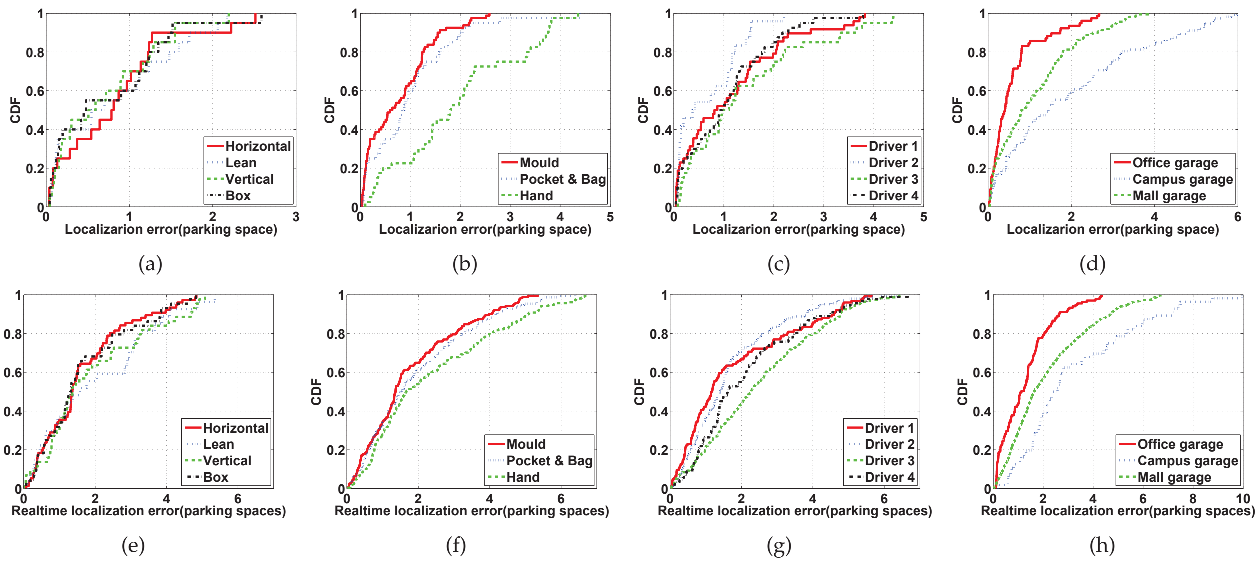

Fig. 17. Final parking location errors (1st row) and realtime tracking location errors (2nd row). (a)(e) 4 phones in the mould. (b)(f) in mould, pocket&bag, and hands. (c)(g) different drivers. (d)(h) different garages.

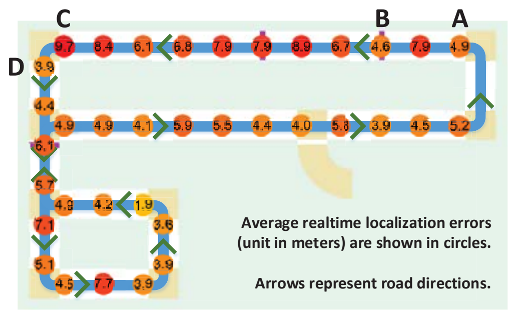
C
B
A
D
Average realtime localization errors (unit in meters) are shown in circles.
Arrows represent road directions.

Fig. 18. Average realtime tracking errors on different garage locations.

mould. They have relatively small errors: all four poses have similar performance, with the 90th percentile error less than 2 parking spaces. The maximum error is less than 3 parking spaces, which is sufficient for remote keys to trigger a honk to locate the car.

Figure 17(b) shows results for different pose categories. Poses in the mould category achieve the best performance, i.e., $\sim$ 2 parking spaces at the 90th percentile, with maximum error of 3 parking spaces. Those in the pocket or bag endure small disturbances thus achieve performance that is a little worse than mould category, i.e., $\sim$ 2 parking spaces at the 90th percentile, with maximum error of 4 parking spaces. Those in hand have largest errors, i.e., $\sim$ 4 parking spaces at the 90th percentile, with maximum error of 5 parking spaces. These larger errors are due to hand disturbances causing more incorrect landmark detections.

We also evaluate the impact of different drivers. Figure 17(c) shows those of two taxi drivers (1 and 3) driving cabs and two volunteer drivers (2 and 4) driving their own cars. The results do not differ too much among different drivers; all have 1.5 $\sim$ 3 parking space errors at the 80th percentile, while the maximum error of 5 parking spaces is from a taxi driver who drives very aggressively, which causes more incorrect detections.

Finally we evaluate impact of the type of parking garage. The 90th percentile errors are around 2,3 and 5 parking spaces, respectively, and maximum errors are 3, 5 and 6 parking spaces, respectively. The difference is caused by different structures. The office garage has best results because it has regular shapes (10(b)) and smooth paved surfaces which minimize road disturbances. The campus garage is the worst because of its irregular shape (10(a)), especially the "Z"-junction of two consecutive turns where many drives take a shortcut instead of two 90-degree turns.

Real time location error. We present the CDFs of real time tracking error in the second row of Figure 17, arranged the same as the first row. The trends are similar in general, but real time errors are generally 50 $\sim$ 100% larger than corresponding parking errors. For example, Figure 17(e) shows all 4 poses in the mould have the 90th percentile error around 4 parking spaces. The maximum error is $\sim$ 5 parking spaces. While those in Figure 17(a) are 2 and 3 parking spaces. Figure 17(f) shows that poses in the mould have the least errors, while those in hand have largest errors, the same trend as Figure 17(b) while all errors are about 60% larger than those in Figure 17(b). Figure 17(g) and (h) are similar as well.

This is because: 1) For final parking location we penalize particles still having non-negligible speeds after the vehicle has stopped. Thus remaining particles are those that have correctly "guessed" the vehicle states. 2) Real time errors include many locations in the middle of long straight driving, where no landmarks are available for calibration. Such locations tend to have larger errors. 3) The vehicle location has much larger uncertainty at the beginning. Thus relatively greater errors are included in real time results. But final location is usually after multiple calibrations, thus better accuracy.

Spatial distribution of real time tracking errors on a garage map with 3 bumps and 8 turns is shown in Figure 18. Each circle has a number, the error averaged over different traces and poses for that location. We observe that in general the error grows on straight paths, and is reduced after encountering landmarks (e.g., from 4.9m after a corner A, growing to 7.9m then reduced to 4.6m after a bump B; 9.7m at C before a corner to 3.9m at D).

The number of particles also impact tracking accuracy. We compare VeTrack with a straightforward baseline that uses 3D tracing and 2D road strips, without two critical components of 2D tracing and 1D roads, Figure 16 shows results for the mall. VeTrack's average localization error quickly converges to $\sim$ 2.5 parking spaces when there are 200 particles (the office and campus garages need only $100 \sim 150$ particles). More particles do not further decrease the error because they are still subject to landmark detection mistakes. The baseline needs about 1000 particles to stabilize, and it is around 5 parking spaces. This shows that VeTrack needs about one order of magnitude less particles, thus ensuring efficient computing for real time tracking on the phone; it also has better accuracy because of the two critical components.

7 Related Work

Phone pose estimation. Existing work [10], [11], [23] estimates the 3D pose of the phone. The latest one, A^3 [14], detects high confidence compass and accelerometer measurements to calibrate accumulative gyroscope errors. The typical approach [10] in vehicular applications is to use the gravity direction as the Z-axis of the vehicle, assuming it is on level ground; gyroscope is used to determine whether the vehicle is driving straight; and the direction of maximum acceleration is assumed to be the Y-axis of the vehicle. As explained in Section 3, it cannot handle vehicles on a slope, and the direction of maximum acceleration may not be vehicle forwarding direction. The estimation also requires long time of unchanged pose, unsuitable under frequent disturbances.

Landmark detection. Distinctive data patterns in different sensing modalities of smartphones have been exploited for purposes including indoor localization [9], [24] and mapping [25]. Similarly, VeTrack detects distinctive inertial sensor patterns by road conditions (e.g., bumps and turns) to calibrate the location estimation. Its algorithms are designed specifically for robustness against noises and disturbances on inertial data from indoor driving.

Dead-reckoning. Dead reckoning is a well explored approach that estimates the future location of a moving object (e.g., ground vehicle [26]) based on its past position and speed. Compared with them, VeTrack does not have special, high precision sensors (e.g., odometer in robotics or radar [26] for ground vehicles), while the required accuracy is much higher than that of aviation.

Dead reckoning has been used for indoor localization using smartphones equipped with multiple inertial sensors [27], [28]. Its main problem is fast error accumulation due to inertial data noises and a lot of work has attempted to mitigate the accumulation. Foot-mounted sensors have been shown effective in reducing the error [29]. Smartphones are more difficult because their poses are unknown and can change. UnLoc [9] replaces GPS with virtual indoor landmarks with unique sensor data patterns for calibration.

To prevent the error accumulation, VeTrack simultaneously harnesses constraints imposed by the map and environment landmarks. Landmark locations most likely remain unchanged for months or even years. The 2D pose estimation handles unknown and possibly changing phone poses. Their output provide calibration opportunities in the SMC framework to minimize error accumulation.

Estimation of vehicle states. There have been many research efforts using smartphones' embedded sensors to monitor the states of vehicles (e.g. dangerous driving alert [7] and CarSafe [30]); sense driver phone use (e.g., car speaker [31]); inspect the road anomaly or conditions (e.g., Pothole Patrol [21]); and detect traffic accidents (Nericell [23] and WreckWatch [32]). The vehicle speed is a critical input in many such applications. While it is easy to calculate the speed using GPS outdoors [33], the signal can be weak or even unavailable for indoor parking lots. Some alternative solutions leverage the phone's signal strength to estimate the vehicle speed [34]. VeTrack uses inertial data only, thus it works without any RF signal or extra sensor instrumentation.

8 Conclusions

In this paper we describe VeTrack which tracks a vehicle's location in real time and records its final parking location. It does not depend on GPS or WiFi signals which may be unavailable, or additional sensors to instrument the indoor environment. VeTrack uses only inertial data, and all sensing/computing happen locally on the phone. It uses a novel shadow trajectory tracing method to convert smartphone movements to vehicle ones. It also detects landmarks such as speed bumps and turns robustly. A probabilistic framework estimates its location under constraints from detected landmarks and garage maps. It also utilizes a 1D skeleton road model to greatly reduce the computing complexity.

Prototype experiments in three parking structures and with several drivers, vehicle make/models have shown that VeTrack can track the vehicle location around a few parking spaces, with negligible latency most of the time. Thus it provides critical indoor location for universal location awareness of drivers. Currently VeTrack still has quite some limitations, such as manual feature design, simultaneous disturbances as discussed previously. We plan to further investigate along these directions to make it mature and practical in the real world.

Acknowledgments

This work is supported in part by NSF CNS 1513719, and NSFC 61625201, 61231010.

References

[1] P. Bahl and V. N. Padmanabhan, "RADAR: An in-building RF-based user location and tracking system," in *IEEE INFOCOM*, 2000, pp. 775–784.

[2] M. Youssef and A. Agrawala, "The horus wlan location determination system," in *ACM MobiSys*, 2005, pp. 205–218.

[3] V. Otsason, A. Varshavsky, A. LaMarca, and E. De Lara, "Accurate gsm indoor localization," in *ACM UbiComp*, 2005, pp. 141–158.

[4] "SFpark," http://sfpark.org/how-it-works/the-sensors/.

[5] "Parking sensors mesh network," http://www.streetline.com/parking-analytics/parking-sensors-mesh-network/.

[6] S. Nawaz, C. Efstratiou, and C. Mascolo, "Parksense: A smartphone based sensing system for on-street parking," in *ACM MobiCom*, 2013, pp. 75–86.

[7] J. Lindqvist and J. Hong, "Undistracted driving: A mobile phone that doesn't distract," in *ACM HotMobile*, 2011, pp. 70–75.

[8] A. Thiagarajan, J. Biagioni, T. Gerlich, and J. Eriksson, "Cooperative transit tracking using smart-phones," in *ACM SenSys*, 2010, pp. 85–98.

[9] H. Wang, S. Sen, A. Elgohary, M. Farid, M. Youssef, and R. R. Choudhury, "No need to war-drive: Unsupervised indoor localization," in *ACM MobiSys*, 2012, pp. 197–210.

[10] Y. Wang, J. Yang, H. Liu, Y. Chen, M. Gruteser, and R. P. Martin, "Sensing vehicle dynamics for determining driver phone use," in *ACM MobiSys*, 2013, pp. 41–54.

[11] J. Yu, H. Zhu, H. Han, Y. J. Chen, J. Yang, Y. Zhu, Z. Chen, G. Xue, and M. Li, "Senspeed: Sensing driving conditions to estimate vehicle speed in urban environments," *IEEE Transactions on Mobile Computing*, vol. 15, no. 1, pp. 202–216, 2016.

[12] M. Zhao, R. Gao, J. Zhu, T. Ye, F. Ye, Y. Wang, K. Bian, G. Luo, and M. Zhang, "Veloc: finding your car in the parking lot," in *ACM SenSys*, 2014, pp. 346–347.

[13] "Apple Developer Center," https://developer.apple.com/.

[14] P. Zhou, M. Li, and G. Shen, "Use it free: Instantly knowing your phone attitude," in *ACM MobiCom*, 2014, pp. 605–616.

[15] S. Thrun, W. Burgard, D. Fox *et al.*, *Probabilistic robotics*. MIT press Cambridge, 2005, vol. 1.

[16] M. de Berg *et al.*, *Computational Geometry*. Springer, 2000, vol. 2.

[17] "Zhang-suen thinning algorithm," http://rosettacode.org/wiki/Zhang-Suen_thinning_algorithm/.

[18] R. Gao, Y. Tian, F. Ye, G. Luo, K. Bian, Y. Wang, T. Wang, and X. Li, "Sextant: Towards ubiquitous indoor localization service by photo-taking of the environment," *IEEE Transactions on Mobile Computing*, vol. 15, no. 2, pp. 460–474, 2016.

[19] S. Preece, J. Goulermas, L. Kenney, and D. Howard, "A comparison of feature extraction methods for the classification of dynamic activities from accelerometer data," *IEEE Transactions on Biomedical Engineering*, vol. 56, no. 3, pp. 871–879, 2009.

[20] C. M. Bishop *et al.*, *Pattern recognition and machine learning*. springer New York, 2006, vol. 1.

[21] J. Eriksson, L. Girod, B. Hull, R. Newton, S. Madden, and H. Balakrishnan, "The pothole patrol: Using a mobile sensor network for road surface monitoring," in *ACM MobiSys*, 2008, pp. 29–39.

[22] K. Li, M. Lu, F. Lu, Q. Lv, L. Shang, and D. Maksimovic, "Personalized driving behavior monitoring and analysis for emerging hybrid vehicles," in *Pervasive Computing*, 2012, pp. 1–19.

[23] P. Mohan, V. N. Padmanabhan, and R. Ramjee, "Nericell: Using mobile smartphones for rich monitoring of road and traffic conditions," in *ACM SenSys*, 2008, pp. 357–358.

[24] M. Azizyan, I. Constandache, and R. Roy Choudhury, "Surroundsense: Mobile phone localization via ambience fingerprinting," in *ACM MobiCom*, 2009, pp. 261–272.

[25] R. Gao, M. Zhao, T. Ye, F. Ye, G. Luo, Y. Wang, K. Bian, T. Wang, and X. Li, "Multi-story indoor floor plan reconstruction via mobile crowdsensing," *IEEE Transactions on Mobile Computing*, vol. 15, no. 6, pp. 1427–1442, 2016.

[26] D. H. Nguyen, J. H. Kay, B. J. Orchard, and R. H. Whiting, "Classification and tracking of moving ground vehicles," *Lincoln Laboratory Journal*, vol. 13, no. 2, pp. 275–308, 2002.

[27] A. Rai, K. K. Chintalapudi, V. N. Padmanabhan, and R. Sen, "Zee: Zero-effort crowdsourcing for indoor localization," in *ACM MobiCom*, 2012, pp. 293–304.

[28] I. Constandache, X. Bao, M. Azizyan, and R. R. Choudhury, "Did you see bob?: Human localization using mobile phones," in *ACM MobiCom*, 2010, pp. 149–160.

[29] P. Robertson, M. Angermann, and B. Krach, "Simultaneous localization and mapping for pedestrians using only foot-mounted inertial sensors," in *ACM UbiComp*, 2009, pp. 93–96.

[30] C.-W. You, N. D. Lane, F. Chen, R. Wang, Z. Chen, T. J. Bao, M. Montes-de Oca, Y. Cheng, M. Lin, L. Torresani, and A. T. Campbell, "Carsafe app: Alerting drowsy and distracted drivers using dual cameras on smartphones," in *ACM MobiSys*, 2013, pp. 461–462.

[31] J. Yang, S. Sidhom, G. Chandrasekaran, T. Vu, H. Liu, N. Cecan, Y. Chen, M. Gruteser, and R. P. Martin, "Sensing driver phone use with acoustic ranging through car speakers," *IEEE Transactions on Mobile Computing*, vol. 11, no. 9, pp. 1426–1440, 2012.

[32] J. White, C. Thompson, H. Turner, B. Dougherty, and D. C. Schmidt, "Wreckwatch: Automatic traffic accident detection and notification with smartphones," *Mob. Netw. Appl.*, vol. 16, no. 3, pp. 285–303, 2011.

[33] B. Hoh, M. Gruteser, R. Herring, J. Ban, D. Work, J.-C. Herrera, A. M. Bayen, M. Annavaram, and Q. Jacobson, "Virtual trip lines for distributed privacy-preserving traffic monitoring," in *ACM MobiSys*, 2008, pp. 15–28.

[34] G. Chandrasekaran, T. Vu, A. Varshavsky, M. Gruteser, R. P. Martin, J. Yang, and Y. Chen, "Vehicular speed estimation using received signal strength from mobile phones," in *ACM UbiComp*, 2010, pp. 237–240.

Ruipeng Gao (M'16) received his B.E. degree in Communication Engineering from Beijing University of Posts and Telecommunications in 2010, and his Ph.D. degree in Computer Science from Peking University in 2016. He is currently a lecturer with the School of Software Engineering, Beijing Jiaotong University, Beijing, China. His research interests include wireless communication and mobile computing.

Mingmin Zhao received the B.S. degree in Computer Science from Peking University in 2015. He is currently working toward the Ph.D. degree in Computer Science and Artificial Intelligence Laboratory at MIT. His research interests include wireless sensing, machine learning, and mobile computing.

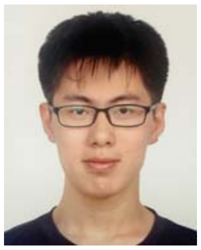

Tao Ye is currently pursuing his B.S. degree in Computer Science from Peking University, Beijing, China. His research interests include mobile computing and artificial intelligence.

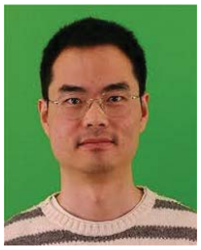

Fan Ye is an Assistant Professor in the ECE department of Stony Brook University. He got his Ph.D. from the Computer Science Department of UCLA, M.S. and B.E. from Tsinghua University. He has published over 60 peer reviewed papers that have received over 7000 citations according to Google Scholar. He has 21 granted/pending US and international patents/applications. His research interests include mobile sensing platforms, systems and applications, Internet-of-Things, indoor location sensing, wireless and sensor networks.

Yizhou Wang is a Professor of Computer Science Department at Peking University, Beijing, China. He received his Bachelors degree in Electrical Engineering from Tsinghua University in 1996, and his Ph.D. in Computer Science from University of UCLA in 2005. Dr. Wang's research interests include computational vision, statistical modeling and learning, pattern analysis, and digital visual arts.

Guojie Luo (M'12) received the B.S. degree in Computer Science from Peking University, Beijing, China, in 2005, and the M.S. and Ph.D. degrees in Computer Science from UCLA, in 2008 and 2011, respectively. He obtained the 2013 ACM SIGDA Outstanding Ph.D. Dissertation Award in Electronic Design Automation and the 10-year Retrospective Most Influential Paper Award at ASP-DAC 2017. He is currently an Assistant Professor in the School of EECS at Peking University. His research interests include FPGA design automation, FPGA acceleration for imaging and sensing, and design technologies for 3D ICs.